Spin-Orbital Entanglement and the Breakdown of Singlets and Triplets in Sr_2RuO_4 Revealed by Spin- and Angle-Resolved Photoemission Spectroscopy

C. N. Veenstra,[1] Z.-H. Zhu,[1] M. Raichle,[1] B. M. Ludbrook,[1] A. Nicolaou,[1,2,7] B. Slomski,[3,4] G. Landolt,[3,4] S. Kittaka,[5,6] Y. Maeno,[5] J. H. Dil,[3,4] I. S. Elfimov,[1,2] M. W. Haverkort,[1,2,7] and A. Damascelli[1,2,*]

[1]*Department of Physics & Astronomy, University of British Columbia, Vancouver, British Columbia V6T 1Z1, Canada*
[2]*Quantum Matter Institute, University of British Columbia, Vancouver, British Columbia V6T 1Z4, Canada*
[3]*Physik-Institut, Winterthurerstrasse 190, Universitat Zürich-Irchel, CH-8057 Zürich, Switzerland*
[4]*Swiss Light Source, Paul Scherrer Institut, CH-5232 Villigen PSI, Switzerland*
[5]*Department of Physics, Graduate School of Science, Kyoto University, Kyoto 606-8502, Japan*
[6]*Institute for Solid State Physics, University of Tokyo, Kashiwa, Chiba 277-8581, Japan*
[7]*Max Planck Institute for Solid State Research, Heisenbergstraße 1, 70569 Stuttgart, Germany*

(Received 10 August 2013; published 26 March 2014)

Spin-orbit coupling has been conjectured to play a key role in the low-energy electronic structure of Sr_2RuO_4. By using circularly polarized light combined with spin- and angle-resolved photoemission spectroscopy, we directly measure the value of the effective spin-orbit coupling to be 130 ± 30 meV. This is even larger than theoretically predicted and comparable to the energy splitting of the d_{xy} and $d_{xz,yz}$ orbitals around the Fermi surface, resulting in a strongly momentum-dependent entanglement of spin and orbital character in the electronic wavefunction. As demonstrated by the spin expectation value $\langle \vec{s_k} \cdot \vec{s_{-k}} \rangle$ calculated for a pair of electrons with zero total momentum, the classification of the Cooper pairs in terms of pure singlets or triplets fundamentally breaks down, necessitating a description of the unconventional superconducting state of Sr_2RuO_4 in terms of these newly found spin-orbital entangled eigenstates.

DOI: 10.1103/PhysRevLett.112.127002 PACS numbers: 74.25.Jb, 74.20.Rp, 74.70.Pq, 79.60.-i

After a flurry of experimental activity [1–5], Sr_2RuO_4 has become a hallmark candidate for spin-triplet chiral p-wave superconductivity, the electronic analogue of superfluid ^{3}He [6–8]. However, despite the apparent existence of such a pairing, some later experiments [9–11] do not fully support this conclusion, as they cannot be explained within a theoretical model using spin-triplet superconductivity alone [12]. A resolution might come from the inclusion of spin-orbit (SO) coupling, which has been conjectured to play a key role in the normal-state electronic structure [13] and may be important when describing superconductivity as well. By mixing the canonical spin eigenstates, the relativistic SO interaction might play a fundamental role beyond simply lifting the degeneracy of competing pairing states [13–17].

Thus far, the experimental study of SO coupling's effects on the electronic structure of Sr_2RuO_4 has been limited to the comparison of band calculations against angle-resolved photoemission spectroscopy (ARPES) [13,18–21] – no success has been obtained in observing experimentally either the strength of SO coupling or its implications for the mixing between spin and orbital descriptions. Here we probe this directly by performing spin-resolved ARPES [22], with circularly polarized light: by using the angular momentum inherent in each photon—along with electric-dipole selection rules [23]—to generate spin-polarized photoemission from the SO mixed states. Combined with a novel spin- and orbitally-resolved *ab initio* based tight-binding (TB) modeling of the electronic structure [24], these results demonstrate the presence of a nontrivial *spin-orbital entanglement* over much of the Fermi surface, i.e., with no simple way of factoring the band states into the spatial and spin sectors. Most importantly, the analysis of the corresponding Cooper pair spin eigenstates establishes the need for a description of the unconventional superconductivity of Sr_2RuO_4 beyond the pure spin-triplet pairing, contrary to what is commonly assumed.

In Sr_2RuO_4 the calculated effective SO coupling is small ($\zeta_{\text{eff}} \sim 90$ meV at the Γ point) with respect to the bandwidth (~3 eV) of the Ru-t_{2g} orbitals, which define the α, β, and γ conduction bands. Nevertheless, its influence always becomes important whenever bands would be degenerate in the absence of SO, either by symmetry or accidentally. This happens at several places in the three-dimensional Brillouin zone, as demonstrated in Figs. 1(a), 1(b) where we show a comparison of the *ab initio*-TB band structure and Fermi surface calculated both with (color) and without (black) SO coupling included [24]. In the absence of SO, by symmetry the d_{xz} and d_{yz} bands would be degenerate along the entire k_z momentum path from Γ to Z [Fig. 1(a)]. Additionally, there are accidental degeneracies along the $k_z = 0$ path from Γ to X, where the bands of $d_{xz,yz}$ and d_{xy} character all cross at momenta near $(2\pi/3, 2\pi/3)$—the exact location of which varies with k_z but often occurs at the Fermi level [Figs. 1(a), 1(b)]. At all these locations SO coupling

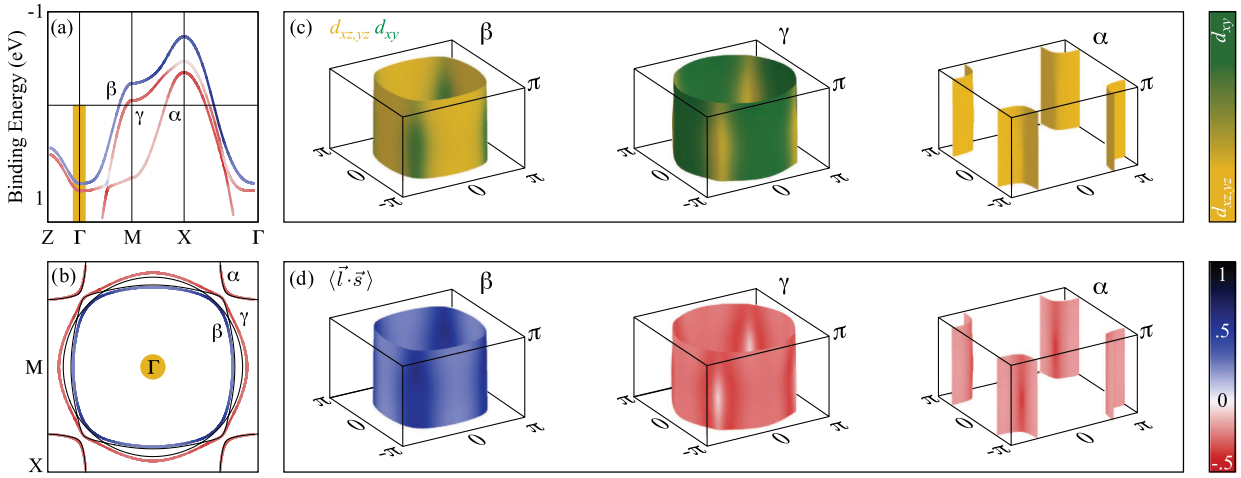

FIG. 1 (color online). (a) Electronic band structure from along the high-symmetry directions and (b) $k_z = 0$ Fermi surface calculated without (thin black) and with (thick, color-coded to show $\langle \vec{l} \cdot \vec{s} \rangle$) the inclusion of SO coupling; at the Γ point, the latter gives rise to a $\zeta_{\text{eff}} \sim 90$ meV splitting [note that $Z \equiv (0, 0, \pi/c)$, $\Gamma \equiv (0, 0, 0)$, $M \equiv (\pi/a, 0, 0)$, $X \equiv (\pi/a, \pi/a, 0)$]. (c,d) Three-dimensional Fermi surface sheets color coded to show (c) orbital character and (d) the expectation value $\langle \vec{l} \cdot \vec{s} \rangle$, in the first Brillouin zone [25]. The energy and momentum location of the spin-resolved ARPES spectra presented in Fig. 2 is marked in yellow in panels (a) and (b).

naturally leads to a splitting [Figs. 1(a), 1(b)] and mixing of the orbital character [Fig. 1(c)] for all three bands.

Interestingly, the effects of SO coupling are not limited to the regions around the nonrelativistic degeneracies since, despite the large bandwidth, the Ru-t_{2g} bands are often separated by energies that are small compared to the SO interaction. The predicted importance of the SO interaction can be directly visualized via the expectation value of $\vec{l} \cdot \vec{s}$ from our *ab initio*-TB modeling, with $\vec{l}$ and $\vec{s}$ being the orbital and spin angular momentum operators. A nonzero value of $\langle \vec{l} \cdot \vec{s} \rangle$ indicates complex orbital eigenstates that can be entangled with the spin. In this case, the wave function cannot be factorized into independent spin and orbital parts, as would be possible for a fully quenched angular momentum (for which $\langle \vec{l} \cdot \vec{s} \rangle = 0$). The calculated $\langle \vec{l} \cdot \vec{s} \rangle$ is shown in Fig. 1 for the high-symmetry dispersion (a), $k_z = 0$ Fermi surface (b), and around the three-dimensional Fermi sheets (d). This suggests SO coupling is important in Sr_2RuO_4 on almost the entire three-sheet Fermi surface [26].

In order to probe the resulting internal spin-orbital structure of the electronic wave function, we turn to spin-resolved ARPES with circularly polarized light: with this technique the circular polarization of the light couples to the angular momentum of the states measured at a given k point, while the spin is resolved directly. A similar approach, albeit without the angular and energy resolution needed to resolve the dispersive states belonging to the conduction band, has been used previously to generate spin-polarized photoemission from materials without a net magnetization, such as GaAs [27] and Ca_2RuO_4 [28]. Here, by exploiting the electron-dipole selection rules for photoemission from conduction-band states selected via spin-resolved ARPES, we directly probe the internal SO structure of the normal state wave function (note that this study is done at ~40 K, thus well above $T_c \simeq 1.5$ K).

To apply this technique on Sr_2RuO_4 we study the SO splitting at the Γ point, $\vec{k} = (0, 0, 0)$, as highlighted in Figs. 1(a), 1(b). This choice is dictated by the need to avoid any intensity contamination from the well-known surface reconstruction of Sr_2RuO_4 [18–20], which leads to the detection of folded bands—preventing a clean spin-ARPES study—anywhere in the Brillouin zone except at the Γ point [24]. In addition, as explained below, this choice selects the experimental geometry and initial-state wave functions that are the most straightforward to analyze, facilitating the direct measurement of both the SO interaction strength and the complex nature of the wave function. At this k point, nonrelativistic band structure calculations predict two degenerate bands of d_{xz} and d_{yz} character, with the d_{xy} band far enough away that it can be ignored (i.e., at about 1.8–2.3 eV higher binding energy, depending on the k_z value). Here SO breaks the degeneracy by hybridizing these bands to form two states with a splitting of $\zeta_{\text{eff}} \sim 90$ meV: a lower binding-energy state with z-components of orbital and spin angular momentum *parallel* $|d^{\downarrow_z}_{-1_z}, d^{\uparrow_z}_{+1_z}\rangle$, and a higher binding-energy state where they are *antiparallel* $|d^{\uparrow_z}_{-1_z}, d^{\downarrow_z}_{+1_z}\rangle$. Here $\uparrow_z$ represents spin, $d_{+1_z} \equiv \sqrt{1/2}(-d_{xz} - id_{yz})$ has $m_{l_z} = 1$, while $d_{-1_z} \equiv \sqrt{1/2}(d_{xz} - id_{yz})$ has $m_{l_z} = -1$. Optical selection rules for the initial-to-final-state excitation with circularly polarized light dictate that both $\Delta\ell = \pm 1$ and $\Delta m_l = \pm 1$. For d orbitals the change in ℓ will favor the $d \to p$ over $d \to f$ transitions, owing to the cross-section at the photon energies used (24 and 56 eV) and in particular the presence of a $d \to f$ Cooper minimum [29] at 47 eV for Ru^{4+} (see also Supplemental Material [24]). The change in m_l will depend on the circular polarization of the photon being right (⊕) or left (⊖). When a ⊕ (⊖) photon is absorbed by the lower binding-energy parallel state $|d^{\downarrow_z}_{-1_z}, d^{\uparrow_z}_{+1_z}\rangle$, m_{l_z} must increase (decrease) by one; but since an $|m_{l_z}| = 2$ final

state is forbidden in the favoured p transition, electrons from the $d^{\downarrow_z}_{-1_z}$ ($d^{\uparrow_z}_{+1_z}$) half of the degenerate state will dominate, resulting in an effective $\downarrow_z$ ($\uparrow_z$) spin polarization. Similarly, photoemission from the higher binding-energy antiparallel state $|d^{\uparrow_z}_{-1_z}, d^{\downarrow_z}_{+1_z}\rangle$ using $\oplus$ ($\ominus$) light will result in photoemission with the opposite spin polarization, $\uparrow_z$ ($\downarrow_z$).

In spin-integrated ARPES [Fig. 2(a)], these Γ-point states are detected as a single broad feature with width ~400 meV [24]; however, it is possible to distinguish them by using circularly polarized light and observing the spin-polarization of the photoelectrons [see schematics in Fig. 2(a)]. The experiment is repeated for both helicities of light, and the results combined to calculate the photoelectron *polarization asymmetry*, which eliminates possible experimental artefacts [24]. This polarization asymmetry is presented in Fig. 2(b): it is zero along x and y crystal axes, and shows a clear wiggle as a function of energy along z, indicating that the photoelectrons have a photon-helicity-dependent spin-polarization only in the z direction. By plotting the intensities corresponding to the observed photoelectron polarization asymmetry for each spatial dimension, Figs. 2(d)–2(f), we can directly resolve these states. For the z direction in Fig. 2(f)—and in particular in Fig. 2(c) where the data have been corrected for light incident at 45° with respect to the spin-orbit quantization axis [24]—they become visible as two energy-split features: $|d^{\downarrow_z}_{-1_z}, d^{\uparrow_z}_{+1_z}\rangle$ photoemits $\downarrow_z$ ($\uparrow_z$) with $\oplus$ ($\ominus$) light, and is thus detected in $I_{\oplus\downarrow,\ominus\uparrow}$; similarly, $|d^{\uparrow_z}_{-1_z}, d^{\downarrow_z}_{+1_z}\rangle$ is detected in $I_{\oplus\uparrow,\ominus\downarrow}$. Along the x and y directions in Figs. 2(d),(e), however, the spectra match the spin-integrated intensity in Fig. 2(a) since the photoelectrons from both states have $\langle s_x\rangle = \langle s_y\rangle = 0$ for both light helicities. The splitting in the z direction is observed with both 24 and 56 eV photons, and its magnitude is 130 ± 30 meV [24], showing a possible enhancement compared to the predicted value $\zeta_{\text{eff}} \sim 90$ meV. Most importantly, the existence of these two states, from which spin-polarized photoemission can be generated using circularly polarized light in the z direction only, is clear experimental evidence of the importance of SO coupling in Sr_2RuO_4 and of its consequences for the complex nature of the normal-state wave functions.

As discussed below, the most important of these consequences is the strong, momentum-dependent, spin-orbital entanglement of the eigenstates around the Fermi surface. This is illustrated in Fig. 3 by plotting the projection of the Bloch wave functions at the Fermi energy onto the Ru-d orbital basis at different momenta [24]. The resulting projections are color coded by the expectation value of the spin operator $\langle s_z\rangle_{(\theta,\phi)}$ for one half of the Kramers-degenerate pair (blue = $\uparrow$, red = $\downarrow$) [30]. Along the edges of the Brillouin zone (M – X) where the bands are well separated, we find particularly in the α band (far right panel in Fig. 3) that the orbitals do not show strong entanglement: each orbital projection is associated with a single expectation value (color) of the spin operator. In addition, the β and α bands are of pure $d_{xz,yz}$ orbital

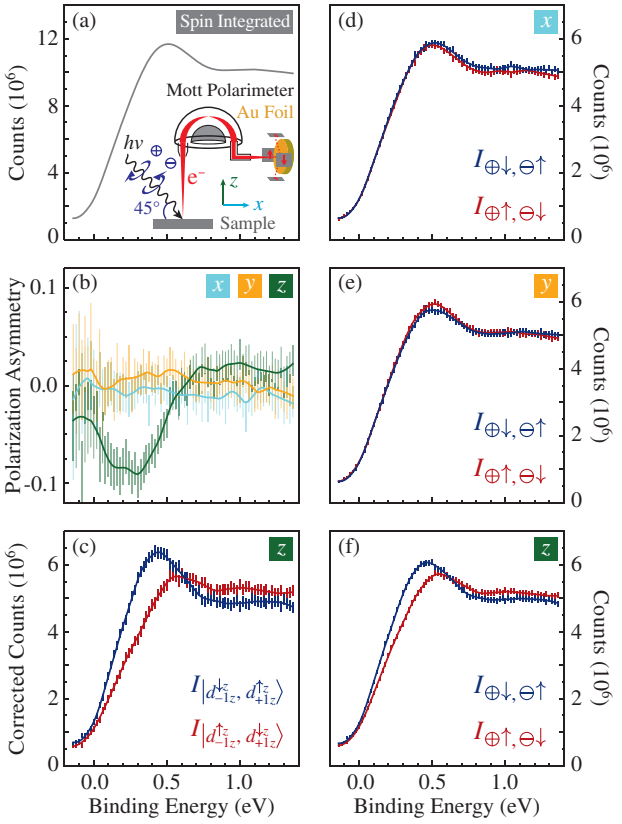

FIG. 2 (color online). (a) Spin-integrated ARPES data measured with 24 eV photons at Γ, as highlighted in Fig. 1. (a,b) Measured polarization asymmetry of the photoemitted electrons, and (d-f) corresponding spin-resolved ARPES intensities for x, y, and z crystal axes, obtained with right ($\oplus$) or left ($\ominus$) circular polarization [see inset of (a) for experiment schematics]. (c) Intensity from each underlying state for the z direction, corrected for light incident at 45° with respect to the spin–orbit quantization axis, as detailed in Supplemental Material [24]. Vertical error bars represent statistical uncertainty based on number of counts in the Mott polarimeters, plotted at 95% confidence together with locally-weighted scatter plot smoothing fits [24].

character, and the γ band of d_{xy} (Fig. 3). Thus at these locations in momentum space the wave function is well approximated by the usual description as a product of independent spatial and spin components,

$$\psi(\mathbf{k},\sigma) = \varphi(\mathbf{k})\phi^{\text{spin}}_{\sigma}, \tag{1}$$

where $\varphi(\mathbf{k})$ and $\phi^{\text{spin}}_{\sigma}$ are the spin and orbital eigenstates, and σ the spin index. However, close to the zone diagonal, e.g., near the intersections of the Fermi sheets with $\Gamma - X$, this is not the case. Here we find strong orbital mixing for all bands and, especially in the γ and β bands, also strong entanglement between orbital and spin character. The orbitals are no longer associated with a uniform spin value; on the contrary, the latter can vary from fully up to fully down along a single orbital projection surface. Here the wave function cannot be written as in Eq. (1), and instead we must use the more general expression,

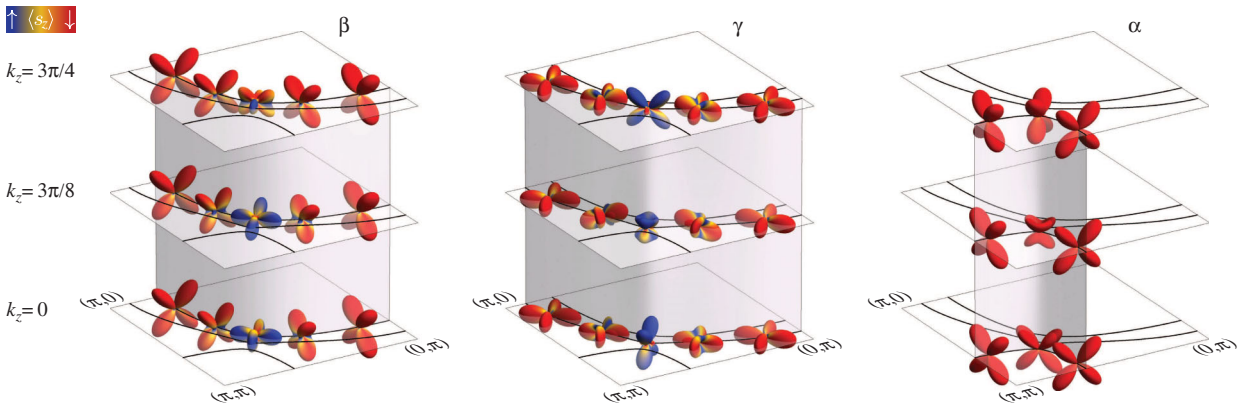

FIG. 3 (color online). Momentum-dependent Ru-d orbital projection of the wave function for the β, γ, and α bands at selected momentum locations along the three-dimensional Fermi surface. The surface color represents the momentum-dependent s_z expectation value along the direction defined by the spherical (θ, ϕ) angles, $\langle s_z \rangle_{(\theta,\phi)}$ [24]; as indicated by the color scale at upper left, blue/red correspond to spin $\uparrow/\downarrow$ for one state of the Kramers-degenerate pair (with the opposite spin state not shown [30]). The strongly mixed colors on some of the orbital projection surfaces for the β and γ bands indicate strong, momentum-dependent spin–orbital entanglement.

$$\psi(\mathbf{k}, \tilde{\sigma}) = c_{\uparrow}\varphi_{\uparrow}(\mathbf{k})\phi_{\uparrow}^{\text{spin}} + c_{\downarrow}\varphi_{\downarrow}(\mathbf{k})\phi_{\downarrow}^{\text{spin}}, \qquad (2)$$

with $\tilde{\sigma}$ being the pseudospin index, and $c_{\uparrow,\downarrow}$ the prefactors of the momentum-dependent spin-orbital entangled eigenstates. Equation (2) further illustrates the nature of the SO-induced entanglement: flipping the spin forces also a change of the orbital character. We note that, due to the nature of the band structure in Sr_2RuO_4, this entanglement is strongly dependent on both $k_{\|}$ and k_z, despite the extremely weak k_z dispersion along the Fermi surface.

A similar momentum and orbital dependence of the spin expectation value is responsible—in topological insulators— for the complex spin texture of the Dirac fermions [31–33]. In Sr_2RuO_4, beyond the normal-state properties, it directly affects the description of superconductivity, as revealed by the inspection of the Cooper pair basic structure. Cooper assumed the two-particle wave function describing a superconducting electron pair to be of the form $\Psi(\mathbf{r}_1, \sigma_1, \mathbf{r}_2, \sigma_2) = \varphi(\mathbf{r}_1 - \mathbf{r}_2)\phi_{\sigma_1,\sigma_2}^{\text{spin}}$, with zero total momentum and the spin part being either singlet (total spin $S = 0$) or triplet ($S = 1$) [34]. This allows one to classify superconductors as a realization of singlet or triplet paired states. However, a fundamental assumption of this description is that one can write the wave function of each electron as a simple product of spatial and spin parts, which is not possible in the case of strong mixing between $\varphi_{\uparrow}(\mathbf{k})$ and $\varphi_{\downarrow}(\mathbf{k})$. Additionally, because of the strong three-dimensional k dependence of this entanglement in Sr_2RuO_4, any transform to pseudospin would also necessarily be k dependent, negating the possibility of using the regular description under a pseudospin basis as might be done, e.g., for the heavy-fermion Ce compounds [35,36]. As a consequence, the classification of Cooper pairs in terms of singlets or triplets fundamentally breaks down for Sr_2RuO_4. This is shown in Fig. 4 for $k_z = 0$ (and in Fig. S5 of the Supplemental Material for the full k_z range [24]), which presents the spin eigenstates available to a pair of electrons with zero total momentum, as obtained from the expectation value $\langle \vec{s_k} \cdot \vec{s_{-k}} \rangle$, plotted versus the Fermi surface angle Θ defined in Fig. 4(d). While familiar singlet and triplet states are seen off the zone diagonal for the α band (with $\langle \vec{s_k} \cdot \vec{s_{-k}} \rangle = -3/4$ and $1/4$, respectively), they are not available for either the β or γ bands, whose spin eigensystem consists of a doublet and two singlets or—depending on the Fermi surface angle Θ—two doublets.

Our findings mark a deviation from a pure spin-triplet pairing for Sr_2RuO_4, since the only portion of the Fermi surface that might support it is contained within the smaller α pocket, and suggest that superconductivity is yet more

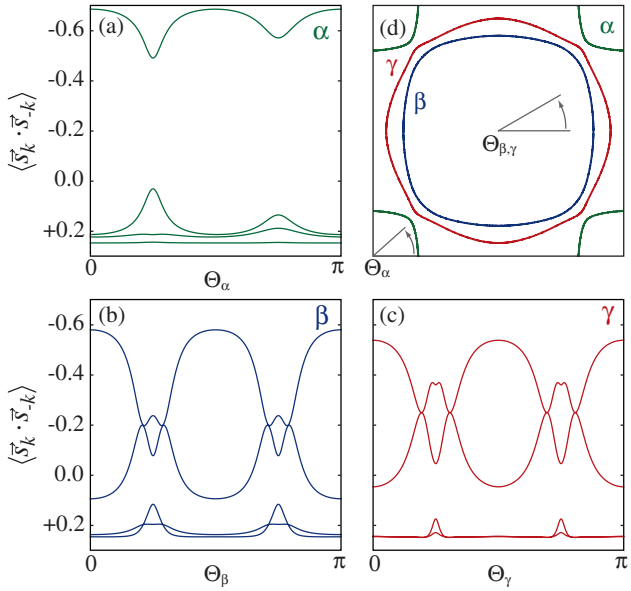

FIG. 4 (color online). Calculated two-particle spin expectation value $\langle \vec{s_k} \cdot \vec{s_{-k}} \rangle$ for states with zero total momentum along the $k_z = 0$ Fermi surface sheets for (a) α, (b) β, and (c) γ bands. The k_x–k_y plane location is defined by the angle Θ for each band, as illustrated in (d). The complete set of results for the full k_z range is shown in Fig. 5S of the Supplemental Material [24].

unconventional than has been assumed so far. This could explain a number of experimental observations at variance with a spin-triplet scenario, such as the extreme sensitivity to field angle of both the magnetic-field-induced second superconducting phase transition [9] and also the suppression of the *ab*-plane upper critical field [10]. These provide evidence for an additional magnetic anisotropy in the superconducting state, of which the entanglement of spin and orbit at the single-particle level would be the natural source. In this regard, it would be interesting to verify what of the chiral *p*-wave superconductor phenomenology [1–5], and apparent conflict in experimental evidence [9–11], would remain when reevaluated in terms of entangled single-particle eigenstates.

We acknowledge R. J. Green, A. Kapitulnik, W. A. MacFarlane, G. A. Sawatzky, P. C. E. Stamp, and L.H. Tjeng for discussions. This work was supported by the Max Planck—UBC Centre for Quantum Materials (A. N., M. W. H.), the Killam, Alfred P. Sloan, Alexander von Humboldt, and NSERC's Steacie Memorial Fellowship Programs (A. D.), the Canada Research Chairs Program (A. D.), NSERC, CFI, CIFAR Quantum Materials, MEXT KAKENHI (No. 22103002), and the Deutsche Forschungsgemeinschaft via Forschergruppe FOR 1346.

*damascelli@physics.ubc.ca

[1] G. M. Luke, Y. Fudamoto, K. M. Kojima, M. I. Larkin, J. Merrin, B. Nachumi, Y. J. Uemura, Y. Maeno, Z. Q. Mao, Y. Mori, H. Nakamura, and M. Sigrist, Nature (London) **394** 558 (1998).
[2] T. M. Riseman, P. G. Kealey, E. M. Forgan, A. P. Mackenzie, L. M. Galvin, A. W. Tyler, S. L. Lee, C. Ager, D. M. Paul, C. M. Aegerter, R. Cubitt, Z. Q. Mao, T. Akima, and Y. Maeno, Nature (London) **396**, 242 (1998).
[3] K. Ishida, H. Mukuda, Y. Kitaoka, K. Asayama, Z. Q. Mao, Y. Mori, and Y. Maeno, Nature (London) **396**, 658 (1998).
[4] K. D. Nelson, Z. Q. Mao, Y. Maeno, and Y. Liu, Science **306**, 1151 (2004).
[5] J. Xia, Y. Maeno, P. T. Beyersdorf, M. M. Fejer, and A. Kapitulnik, Phys. Rev. Lett. **97**, 167002 (2006).
[6] T. M. Rice and M. Sigrist, J. Phys. Condens. Matter **7**, L643 (1995).
[7] M. Rice, Nature (London) **396**, 627 (1998).
[8] A. P. Mackenzie and Y. Maeno, Rev. Mod. Phys. **75**, 657 (2003).
[9] Z. Q. Mao, Y. Maeno, S. NishiZaki, T. Akima, and T. Ishiguro, Phys. Rev. Lett. **84**, 991 (2000).
[10] S. Kittaka, T. Nakamura, Y. Aono, S. Yonezawa, K. Ishida, and Y. Maeno, Phys. Rev. B **80**, 174514 (2009).
[11] S. Yonezawa, T. Kajikawa, and Y. Maeno, Phys. Rev. Lett. **110**, 077003 (2013).
[12] Y. Maeno, S. Kittaka, T. Nomura, S. Yonezawa, and K. Ishida, J. Phys. Soc. Jpn. **81**, 011009 (2012).
[13] M. W. Haverkort, I. S. Elfimov, L. H. Tjeng, G. A. Sawatzky, and A. Damascelli, Phys. Rev. Lett. **101**, 026406 (2008).
[14] K. K. Ng and M. Sigrist, Europhys. Lett. **49**, 473 (2000).
[15] S. Raghu, A. Kapitulnik, and S. A. Kivelson, Phys. Rev. Lett. **105**, 136401 (2010).
[16] J. J. Deisz and T. E. Kidd, Phys. Rev. Lett. **107**, 277003 (2011).
[17] C. M. Puetter and H.-Y. Kee, Europhys. Lett. **98**, 27010 (2012).
[18] A. Damascelli, D. H. Lu, K. M. Shen, N. P. Armitage, F. Ronning, D. L. Feng, C. Kim, Z.-X. Shen, T. Kimura, Y. Tokura, Z. Q. Mao, and Y. Maeno, Phys. Rev. Lett. **85**, 5194 (2000).
[19] K. M. Shen, A. Damascelli, D. H. Lu, N. P. Armitage, F. Ronning, D. L. Feng, C. Kim, Z.-X. Shen, D. J. Singh, I. I. Mazin, S. Nakatsuji, Z. Q. Mao, Y. Maeno, T. Kimura, and Y. Tokura, Phys. Rev. B **64**, 180502 (2001).
[20] C. N. Veenstra, Z.-H. Zhu, B. Ludbrook, M. Capsoni, G. Levy, A. Nicolaou, J. A. Rosen, R. Comin, S. Kittaka, Y. Maeno, I. S. Elfimov, and A. Damascelli, Phys. Rev. Lett. **110**, 097004 (2013).
[21] H. Iwasawa, Y. Yoshida, I. Hase, S. Koikegami, H. Hayashi, J. Jiang, K. Shimada, H. Namatame, M. Taniguchi, and Y. Aiura, Phys. Rev. Lett. **105**, 226406 (2010).
[22] J. Osterwalder, Lect. Notes Phys. **697**, 95 (2006).
[23] A. Damascelli, Phys. Scr. **T109**, 61 (2004).
[24] See Supplemental Material at http://link.aps.org/supplemental/10.1103/PhysRevLett.112.127002 for methods, additional experimental data, calculation details, the Mathematica notebook for the spin- and orbitally-resolved *ab initio* tight-binding Hamiltonian used here, and the complete k_z-dependent results for $\langle \vec{s_k} \cdot \vec{s_{-k}} \rangle$.
[25] See also Fig. S1 in Supplemental Material http://link.aps.org/supplemental/10.1103/PhysRevLett.112.127002, which presents the three-dimensional evolution of the Fermi surface in the conventional Brillouin zone derived from the body-centered tetragonal unit cell of Sr_2RuO_4.
[26] We also note that $\langle \vec{l} \cdot \vec{s} \rangle = 0$ does not necessarily imply that SO coupling is not important; while the eigenstates may still be entangled, the individual $\vec{l} \cdot \vec{s}$ vector components might simply sum to zero, as is the case for the bulges of the γ band near the zone diagonals [24].
[27] D. T. Pierce and F. Meier, Phys. Rev. B **13**, 5484 (1976).
[28] T. Mizokawa, L. H. Tjeng, G. A. Sawatzky, G. Ghiringhelli, O. Tjernberg, N. B. Brookes, H. Fukazawa, S. Nakatsuji, and Y. Maeno, Phys. Rev. Lett. **87**, 077202 (2001).
[29] J. W. Cooper, Phys. Rev. **128**, 681 (1962).
[30] Note that the two states of each Kramers-degenerate pair have opposite spin polarization, consistent with the absence of net spin polarization at any k point in Sr_2RuO_4.
[31] M. Hasan and C. Kane, Rev. Mod. Phys. **82**, 3045 (2010).
[32] Z.-H. Zhu, C. N. Veenstra, G. Levy, A. Ubaldini, P. Syers, N. P. Butch, J. Paglione, M. W. Haverkort, I. S. Elfimov, and A. Damascelli, Phys. Rev. Lett. **110**, 216401 (2013).
[33] Z.-H. Zhu, C. N. Veenstra, S. Zhdanovich, M. Schneider, T. Okuda, K. Miyamoto, S.-Y. Zhu, H. Namatame, M. Taniguchi, M. W. Haverkort, I. S. Elfimov, and A. Damascelli, Phys. Rev. Lett. **112**, 076802 (2014).
[34] J. Bardeen, L. N. Cooper, and J. R. Schrieffer, Phys. Rev. **108** 1175 (1957).
[35] H. Mukuda, T. Ohara, M. Yashima, Y. Kitaoka, R. Settai, Y.OnukiK. M. Itoh, and E. E. Haller, Phys. Rev. Lett. **104**, 017002 (2010).
[36] In heavy-fermion compounds the SO coupling is much larger than the bandwidth, suppressing the momentum dependence of the pseudospin transform and enabling a pseudospin description of superconductivity.

Supplemental Material for:

Spin-Orbital Entanglement and the Breakdown of Singlets and Triplets in Sr_2RuO_4 Revealed by Spin- and Angle-Resolved Photoemission Spectroscopy

C. N. Veenstra, Z.-H. Zhu, M. Raichle, B. M. Ludbrook, A. Nicolaou, B. Slomski, G. Landolt, S. Kittaka, Y. Maeno, J. H. Dil, I. S. Elfimov, M. W. Haverkort, and A. Damascelli

Methods

Spin-resolved ARPES experiments. The measurements were performed on the normal state of Sr_2RuO_4 at the Swiss Light Source using the COPHEE endstation on the Surface and Interface Spectroscopy beamline, with ∼100 meV energy resolution and ∼1° angular resolution (the latter is equivalent to $\sim 0.1\,\pi/a$ at 24 eV and $\sim 0.2\,\pi/a$ at 56 eV photon energy), which allows the selection of electrons in energy-momentum space. These electrons are deflected into an array of Mott detectors, where the spin polarization can be resolved in all three spatial dimensions. High-quality Sr_2RuO_4 single crystals with no 3 K phase contamination [1] were cleaved in situ at 40 K and base pressures in the 10^{-9} mbar range. Owing to the relatively high temperature and pressure, no features associated with the reconstructed surface were detected [1]. All measurements were repeated using the beamline's elliptically-polarizing undulator to generate both right ($\oplus$) and left ($\ominus$) circularly polarized light, and the photoelectron polarization asymmetry $P^{\otimes}$ was calculated using the geometric formula [2] to eliminate the effects of circular dichroism (Supplementary Information):

$$P^{\otimes} S_{\mathrm{Motts}} = \frac{\sqrt{I_U^{\oplus} I_D^{\ominus}} - \sqrt{I_D^{\oplus} I_U^{\ominus}}}{\sqrt{I_U^{\oplus} I_D^{\ominus}} + \sqrt{I_D^{\oplus} I_U^{\ominus}}}\,. \tag{S1}$$

Here S_{Motts} is the empirically determined measure of the efficiency of a Mott spin-detector pair (the so-called Sherman function), and I is the intensity for the up (U) and down (D) halves of the Mott pair measured with circular plus ($\oplus$) and minus ($\ominus$) light. This formula was used for each of the Mott polarimeter pairs and the resulting polarization asymmetry was then translated into sample coordinates according to the experimental geometry. With the effects of dichroism eliminated, this photoelectron polarization asymmetry is equivalent to the true energy- and k-resolved photon-helicity-dependent electron spin polarization.

Electronic structure calculations. To theoretically study the effects of the SO interaction on the low-energy electronic states of Sr_2RuO_4, and in particular the momentum-dependent spin–orbital entanglement, the bulk band structure was calculated using the linear muffin-tin orbital (LMTO) code, which was tested against that calculated with full-potential linearized augmented-plane-wave method using WIEN2k. The parameters were extracted from the LMTO results using the order-N muffin-tin orbital method [3] on the minimal basis of oxygen $2p$ and ruthenium $4d$ orbitals. Atomic SO coupling was then added as a local term in the Hamiltonian, the results of which show excellent agreement with the Fermi surface and band dispersion obtained from relativistic (i.e., SO included) calculations in WIEN2k. The orbitals in Fig. 3 depict the (θ, ϕ) angular dependence of the Ru-d orbital projection of the Bloch wavefunctions for a given momentum at the Fermi energy. Shown is the surface defined by the equation $r(\theta,\phi) = \sum_{\tau,\tau'} Z_\tau(\theta,\phi) Z_{\tau'}(\theta,\phi) \langle a^\dagger_{i,\tau,k} a_{i,\tau',k} \rangle$, where i and τ are the band and Ru-d orbital indexes, k is the momentum of the Bloch eigenstate, and Z are the cubic harmonics. The surface color corresponds to the momentum-dependent s_z expectation value along the direction defined by the spherical (θ, ϕ) angles, $\langle s_z \rangle_{(\theta,\phi)} = \sum_{\tau,\tau'} Z_\tau(\theta,\phi) Z_{\tau'}(\theta,\phi) \frac{1}{2} \left\langle a^\dagger_{i,\tau,k,\uparrow} a_{i,\tau,k,\uparrow} - a^\dagger_{i,\tau,k,\downarrow} a_{i,\tau,k,\downarrow} \right\rangle$, with only one of the two Kramers degenerate states shown (the other having opposite spin polarization).

Components of $\langle \vec{l} \cdot \vec{s} \rangle$ around the Fermi surface

In order to investigate the coupling between the spin and orbital angular momentum near the Fermi energy in Sr_2RuO_4 we plot the expectation value of their dot product, $\langle \vec{l} \cdot \vec{s} \rangle$, for the states around the Fermi surface sheets. In a system without spin–orbit (SO) coupling, the independence of these two vectors would cause this expectation value to be zero everywhere. In Fig. S1(b) we show $\langle \vec{l} \cdot \vec{s} \rangle$, contrasted against the orbital character in (a), as presented in the main text. In (a) we see how the β and α bands are of mostly d_{xz} and d_{yz} character, while the γ band is of mostly d_{xy} character; the exception is near the anticrossing of the β and γ bands close to $(\frac{2\pi}{3}, \frac{2\pi}{3})$ where the strongest mixing occurs and their orbital character changes. In (b) we see that, despite the apparent mixing only at the anticrossing noted in (a), spin and orbital angular momentum remain coupled around almost the entire Fermi surface, as evidenced by the non-zero value of $\langle \vec{l} \cdot \vec{s} \rangle$. Interestingly, we find that $\langle \vec{l} \cdot \vec{s} \rangle = 0$ only near the small portion of the γ band which is of d_{xz}/d_{yz} character. However, in (c-e) we see that this is not because spin and orbit are independent at this location in momentum space; instead we see, in (e) for the z direction especially, that $\vec{l}$ and $\vec{s}$ are just as strongly coupled in this location but that $\langle \vec{l} \cdot \vec{s} \rangle = 0$ only as a sum of non-zero components. This

demonstrates that the spin and orbital angular momentum are coupled everywhere on the Fermi surface, for all three Ru-t_{2g} conduction bands.

High resolution ARPES data

In addition to the spin-resolved data presented in the main text, higher-resolution angle-resolved photoemission spectroscopy (ARPES) experiments were performed at the University of British Columbia. In Fig S2 we present some of these data taken at 5.2 K, under vacuum with pressure in the 10^{-11} mbar range, using the 21.22 eV He I spectral line, and resolutions of $\sim$17 meV and $\sim 0.01\,\frac{\pi}{a}$ angular equivalent. Fig S2(a) shows an energy distribution curve (EDC) taken at the exact same spot in 2D momentum space as that measured with spin-ARPES and presented in the main text, while Fig S2(b) shows its location in momentum space on the measured band map and Fermi surface. These data demonstrate that the two states studied by spin-ARPES and presented in the main text have a fundamentally broad lineshape – even with a resolution approximately seven times smaller than the splitting their separation cannot be resolved without circularly polarized light and spin discrimination. Note that this sample, cleaved at lower temperature and in better vacuum conditions, shows clear evidence of the reconstructed surface electronic structure [4, 1] (as seen by the folded α' band), while that presented in the main text did not. In either case no additional folded features will appear in the studied EDC at the Γ point, owing to the nature of the folding which maps the X point (which has no features in that energy range) to the Γ point – an additional benefit of performing the experiment at this location in momentum space.

Photoionization cross-sections for $d\rightarrow p$ and $d\rightarrow f$ transitions

In the analysis of the spin-resolved ARPES data measured with circular polarization we referred to the dominance of the $d\rightarrow p$ over $d\rightarrow f$ transitions. While at 54 eV photon energy this dominance directly stems from the relative magnitude of the photoionization cross-sections, at 24 eV it requires additional considerations. First we note that the $d\rightarrow f$ photoionization cross section for Ru^{4+} presents a Cooper minimum at 47 eV; this suppresses the photoemission intensity in the $d\rightarrow f$ channel all the way to zero at 47 eV, and makes it negligible compared to the $d\rightarrow p$ channel in the 30-60 eV range. In particular, at the 56 eV photon energy used for the data in Fig. S4, the difference in cross section is about one order of magnitude and the $d\rightarrow f$ contribution can be disregarded. Second, in regard to the 24 eV data in Fig. 2 and S3, we note that at 20-30 eV the photoionization cross sections for the two channels start becoming comparable; nevertheless, as discussed below, $d\rightarrow p$ still dominates

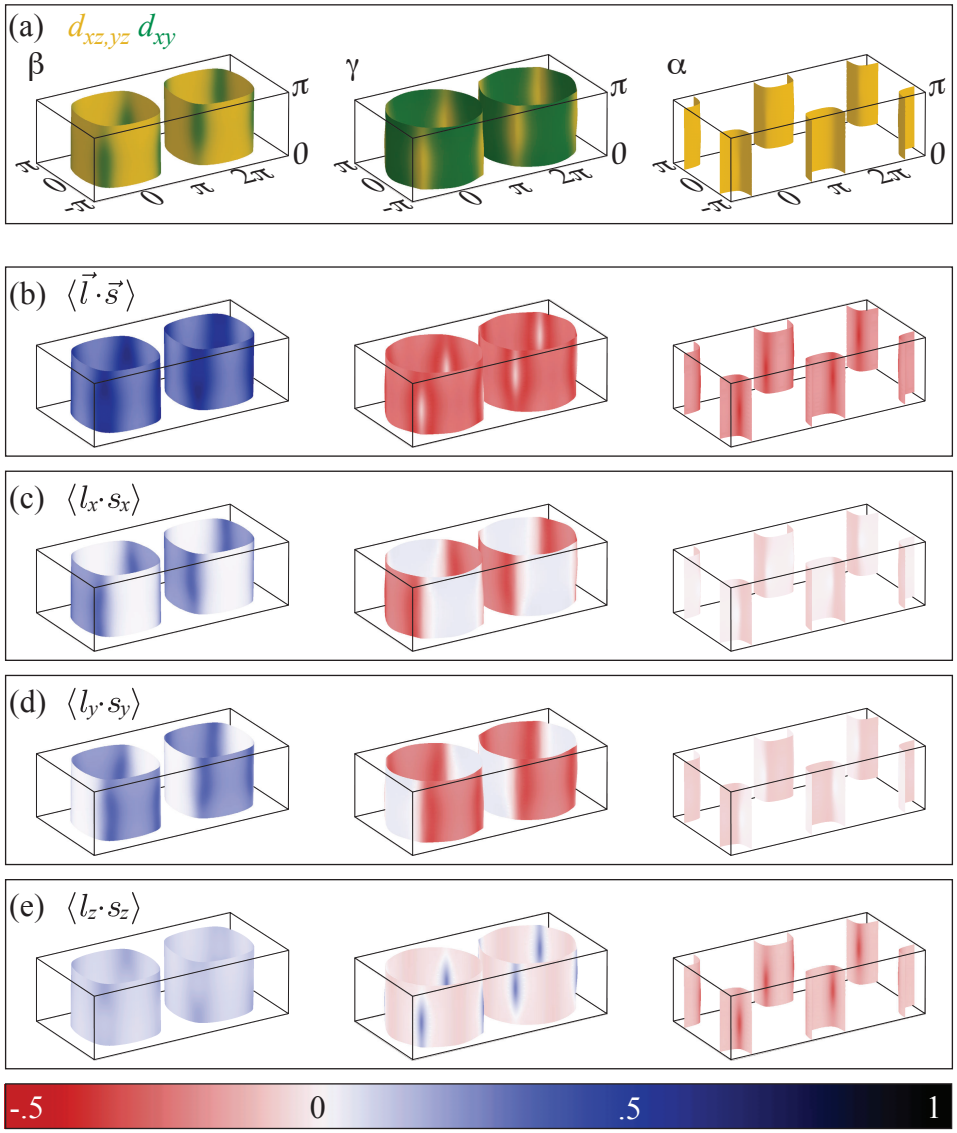

Figure S1: The Fermi surface sheets of Sr_2RuO_4 colorized to show (a) orbital character, as well as (b) $\langle \vec{l} \cdot \vec{s} \rangle$ and its components (c-e) along the three crystal axes (for the latter the color scale is shown at the bottom). The extended zone scheme is used to illustrate the conventional Brillouin zone in the fundamentally body-centered tetragonal unit cell.

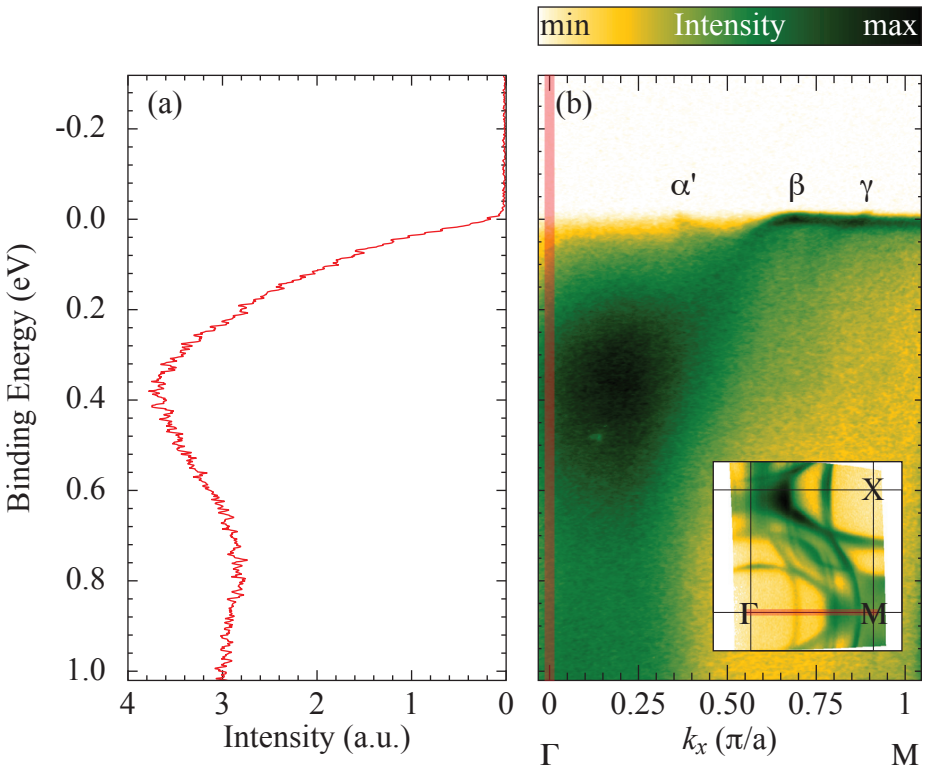

Figure S2: ARPES on Sr_2RuO_4 at the Γ point; (a) shows an EDC integrated over $\sim 0.03\,\frac{\pi}{a}$ around the Γ point, as marked in the band map of panel (b). In (b) bands are labelled as they cross the Fermi level (with primes denoting reconstructed features [1]); the location of the band map is marked on the Fermi surface map shown in the inset.

over $d \rightarrow f$ in spin-resolved photoemission with circular polarized light. Because transitions to an $|m_{l_z}| = 2$ final state are strictly forbidden in the $d \rightarrow p$ channel, it follows that $d \rightarrow p$ photoionization leads to photoemission only from a single state of either Γ-point doublets – and thus to a maximal spin-polarized signal. In the $d \rightarrow f$ channel, instead, both states of each doublet – with their opposite spins – can photoemit, giving rise to canceling photoemission intensities and a corresponding spin-independent background. The cancellation is however not complete because of the asymmetry between transitions to f final states with $|m_{l_z}| = 2$ or 0. These $d \rightarrow f$ transitions partially reduce the spin-polarization by equal amounts from both spin-up and spin-down $d \rightarrow p$ channels. As a net result, this remnant f-channel contribution simply leads to a reduced separation for parallel- and antiparallel-intensity peaks in spin-resolved ARPES, consistent with the experimental observation of a smaller Γ-point splitting at 24 than at 56 eV, which will be discussed in the following.

Polarization asymmetry and the angle of incidence in spin-ARPES

The geometric polarization asymmetry [2], defined as in the main text in terms of the intensities (I) from the up (U) and down (D) detectors for circular right ($\oplus$) and left ($\ominus$) light, is given by the following expression:

$$P^{\otimes} S_{\text{Motts}} = \frac{\sqrt{I_U^{\oplus} I_D^{\ominus}} - \sqrt{I_D^{\oplus} I_U^{\ominus}}}{\sqrt{I_U^{\oplus} I_D^{\ominus}} + \sqrt{I_D^{\oplus} I_U^{\ominus}}}, \tag{S2}$$

which eliminates the effects of circular dichroism and any response imbalance that might exist between the two detectors in the Mott pair (the Sherman "function", S_{Motts}, is a measure of the efficiency of spin discrimination and is a constant, which we ignore here for simplicity). The effectiveness of Eq. S2 can be seen by modelling the measured intensities as:

$$\begin{aligned} I_U^{\oplus} &= d^{\oplus} r_U I_{\oplus\uparrow,\ominus\downarrow} \\ I_D^{\ominus} &= d^{\ominus} r_D I_{\oplus\uparrow,\ominus\downarrow} \\ I_D^{\oplus} &= d^{\oplus} r_D I_{\oplus\downarrow,\ominus\uparrow} \\ I_U^{\ominus} &= d^{\ominus} r_U I_{\oplus\downarrow,\ominus\uparrow}\,. \end{aligned} \tag{S3}$$

Here the d and r terms account for the circular dichroism and detector response rates and $I_{\oplus\uparrow,\ominus\downarrow} \equiv I_{\oplus\uparrow} = I_{\ominus\downarrow}$ (and its opposite, $I_{\oplus\downarrow,\ominus\uparrow}$) are the fundamental photoemission intensities we are interested in, whose spin polarization changes sign upon switching the helicity of the incident light. By substitution we see that the dichroism and detector efficiencies cancel out, and the polarization asymmetry reverts to the simple form:

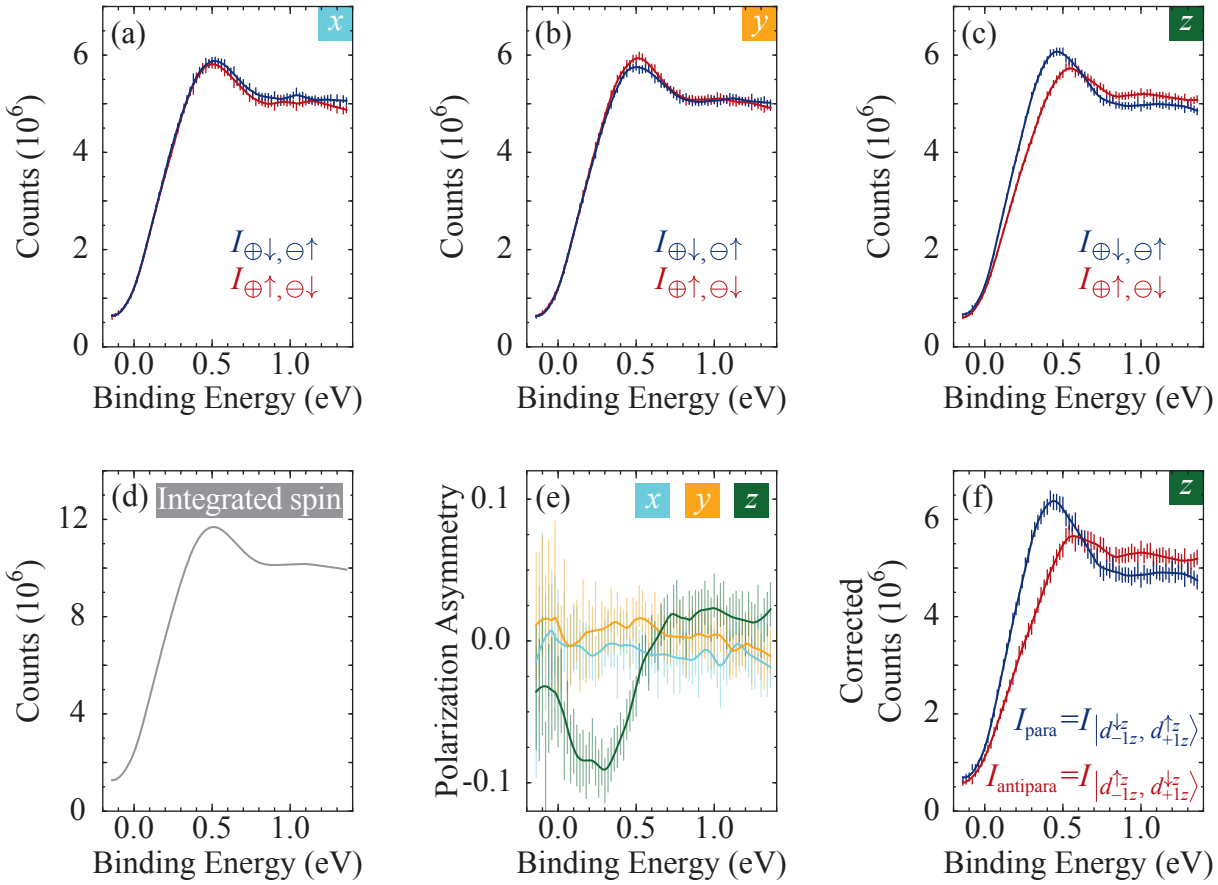

Figure S3: Spin-ARPES using 24eV circularly polarized light on Sr_2RuO_4 at the Γ point. (a-c) Spin-ARPES intensities relative to each of the crystal axes obtained with right (⊕) or left (⊖) circularly polarized light; these are derived, according to Eq. S5, from the integrated spin data and measured polarization asymmetry shown in panel (d) and (e). (f) Intensity from each underlying state, corrected for light incident at 45° with respect to the spin–orbit quantization axis and assuming no background, according to Eq. S7. Error bars represent statistical uncertainty based on number of counts in the Mott Polarimeters, plotted at 95% confidence, with locally weighted scatterplot smoothing fits shown [5].

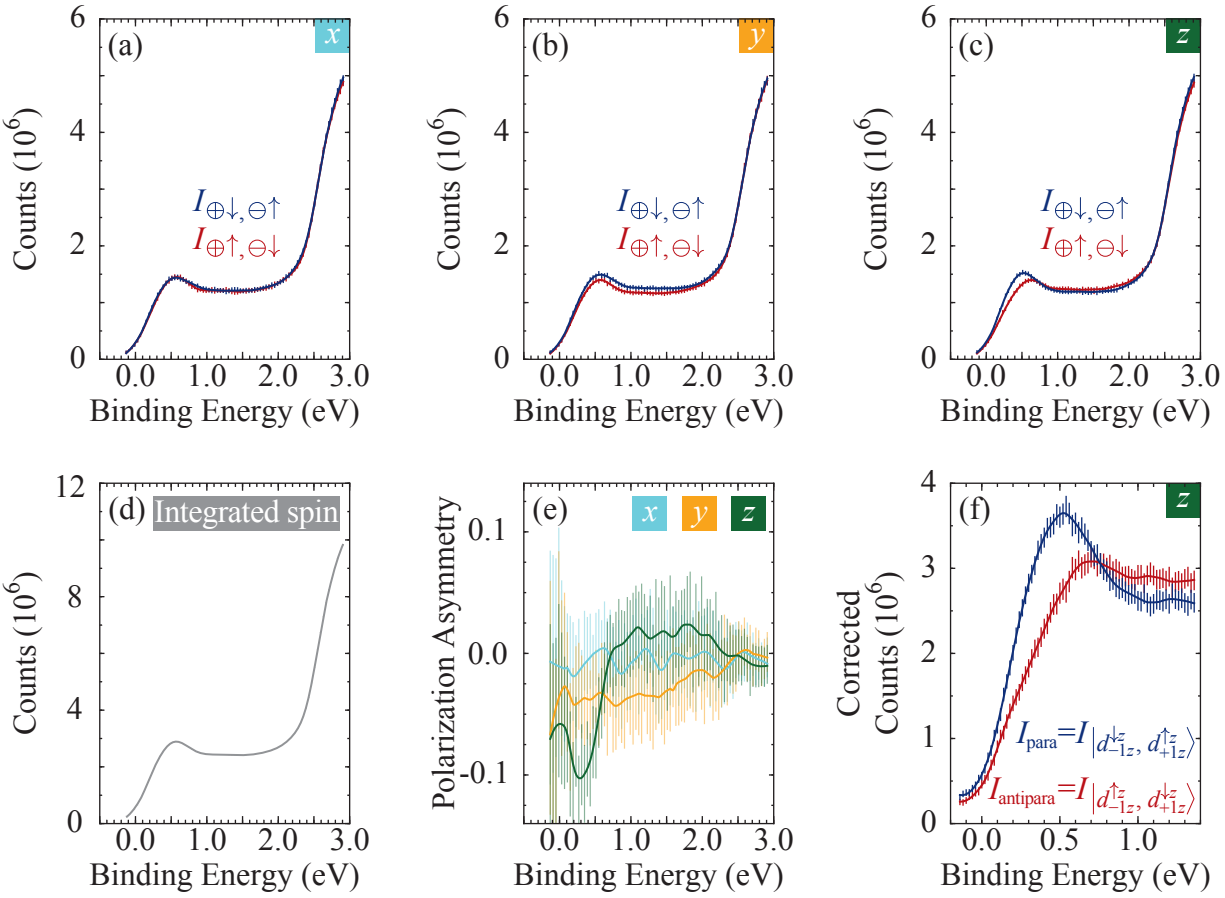

Figure S4: Spin-ARPES using 56eV circularly polarized light on Sr_2RuO_4 at the Γ point, and taken over a larger energy range than Fig. S3; this wider range shows that the polarization asymmetry goes to zero at the non-SO split higher binding-energy states. (a-c) Spin-ARPES intensities relative to each of the crystal axes obtained with right ($\oplus$) or left ($\ominus$) circularly polarized light; these are derived, according to Eq. S5, from the integrated spin data and measured polarization asymmetry shown in panel (d) and (e). (f) Close-up in energy of the intensity from each underlying state, corrected for light incident at 45° with respect to the spin–orbit quantization axis and assuming no background, according to Eq. S7; this panel is taken from an additional data set with narrower energy binning. Error bars represent statistical uncertainty based on number of counts in the Mott Polarimeters, plotted at 95% confidence, with locally weighted scatterplot smoothing fits shown [5].

$$P^{\otimes} = \frac{I_{\oplus\uparrow,\ominus\downarrow} - I_{\oplus\downarrow,\ominus\uparrow}}{I_{\oplus\uparrow,\ominus\downarrow} + I_{\oplus\downarrow,\ominus\uparrow}}\,. \tag{S4}$$

The total intensity (I_T) can thus be combined with the measured polarization asymmetry to reconstruct the spin intensities for each spatial direction according to:

$$\begin{aligned} I_{\oplus\uparrow,\ominus\downarrow} &= I_T(1 + P^{\otimes})/2 \\ I_{\oplus\downarrow,\ominus\uparrow} &= I_T(1 - P^{\otimes})/2\,. \end{aligned} \tag{S5}$$

These are the spin intensities shown in Figs. S3(a-c) and S4(a-c) for the two measured photon energies of 24 and 56 eV, as constructed directly from the integrated spin (d) and polarization asymmetry (e). From these datasets two distinct features, split in the z direction only, are already apparent (we also note that, while similar in all respects, the wider binding energy range 56 eV data show that the polarization asymmetry vanishes at the non-SO split, high-energy oxygen states). However, owing to the experimental geometry (light incident at 45° relative to the analyzer), photons cannot be incident directly along the z direction (additionally there is a node in the final state preventing the experiment from being performed in the second Brillouin zone with normal incident light and 45° emission). The result is that with equal probability the photons will interact either with m_{l_z}, resulting in spin-polarized photoemission from the states with parallel and antiparallel spin and orbital angular momentum (as described in the main text), or with m_{l_x}, resulting in non-polarized photoemission from both states (which will be measured as either $\uparrow$ or $\downarrow$ with equal probability). Therefore, in the z direction, the spin intensity measured for each configuration in terms of these underlying states will be given by:

$$\begin{aligned} I_{\oplus\downarrow,\ominus\uparrow} &= \frac{I_{\text{parallel}}}{2} + \frac{I_{\text{parallel}}}{4} + \frac{I_{\text{antiparallel}}}{4} \\ I_{\oplus\uparrow,\ominus\downarrow} &= \frac{I_{\text{antiparallel}}}{2} + \frac{I_{\text{antiparallel}}}{4} + \frac{I_{\text{parallel}}}{4}\,. \end{aligned} \tag{S6}$$

Here I_{parallel} and $I_{\text{antiparallel}}$ represent the total photoemission intensity given off by the states discussed in the main text; the single terms on the left represent the spin-polarized photoemission described in the main text (divided by two due to only half of the photons interacting with m_{l_z}), while the two terms on the right represent the non-spin-polarized photoemission (divided by four due to half photons interacting with m_{l_x}, and half of those being measured as either up or down). This dilution causes a decrease in the observed splitting compared to the intrinsic one, which can be corrected by taking:

$$I_{\text{parallel}} = (3I_{\oplus\downarrow,\ominus\uparrow} - 1I_{\oplus\uparrow,\ominus\downarrow})/2 = I_T(1 - 2P^{\otimes})/2$$
$$I_{\text{antiparallel}} = (3I_{\oplus\uparrow,\ominus\downarrow} - 1I_{\oplus\downarrow,\ominus\uparrow})/2 = I_T(1 + 2P^{\otimes})/2 \quad \text{(S7)}$$

to recover the intensities from each state; this assumes that all observed intensity is from only these two states with no background. Such a correction is shown in Fig. S3(f) and S4(f), as well as Fig. 2(d) of the main text, and returns a larger splitting.

Observing the uncorrected splitting at the different photon energies and energy ranges measured results in estimates of 83 meV (at 24 eV photon energy), and 101 meV and 110 meV (at 56 eV photon energy), for an average of 98 ± 14 meV. However, this estimate *must* be low due to the experimental geometry and its effect as described above. Using the correction, as described above, on the same data sets results in estimates of 125 meV (at 24 eV), and 184 meV and 172 meV (at 56 eV), for an average of 160 ± 30 meV. However, this estimate *may* be high, as it assumes that all intensity arises from these two states with no background. These limits therefore represent upper and lower bounds of the intrinsic splitting between these two states, for an overall estimate of 130 ± 30 meV.

Available spin-eigenstates around the Fermi surface

Thus far we have examined only single-particle properties, however, without making any assumptions about the pairing mechanism, we may also use our model to examine the spin-eigenstates available to a pair of electrons with 0 net momentum – one electron at k and one at $-k$. These eigenstates are shown in Fig. S5 by plotting the expectation value of $\vec{s_k} \cdot \vec{s_{-k}}$ around the Fermi surface sheets for all bands at three k_z values. Pure, uncoupled, spins will form the familiar singlet/triplet eigensystem, which is visible at a single state with $\langle \vec{s_k} \cdot \vec{s_{-k}} \rangle = -\frac{3}{4}$ and a triplet of states with $\langle \vec{s_k} \cdot \vec{s_{-k}} \rangle = \frac{1}{4}$; such a system can be seen to occur off the zone diagonal for the α band in Fig. S5(c,f,i). However, a singlet/triplet eigensystem is not available for either the β or γ bands anywhere in momentum space, as seen in Fig. S5(a,d,g) and (b,e,h), respectively; instead the available eigensystem is observed to be either a doublet and two singlets, or two doublets, depending on the location in k-space. In this regard, we also note that the introduction of a momentum-dependent pseudo-spin would not resolve this issue, since the unitary transformation $\tilde{\sigma} = \mathcal{U}(\mathbf{k})\,\sigma$ that in a momentum-dependent fashion links the spin and pseudo-spin for the one-particle eigenstates also enters in the spin operator, $\tilde{s} = \mathcal{U}^{\dagger}(\mathbf{k})\,s\,\mathcal{U}(\mathbf{k})$, thereby leaving the expectation values unaltered.

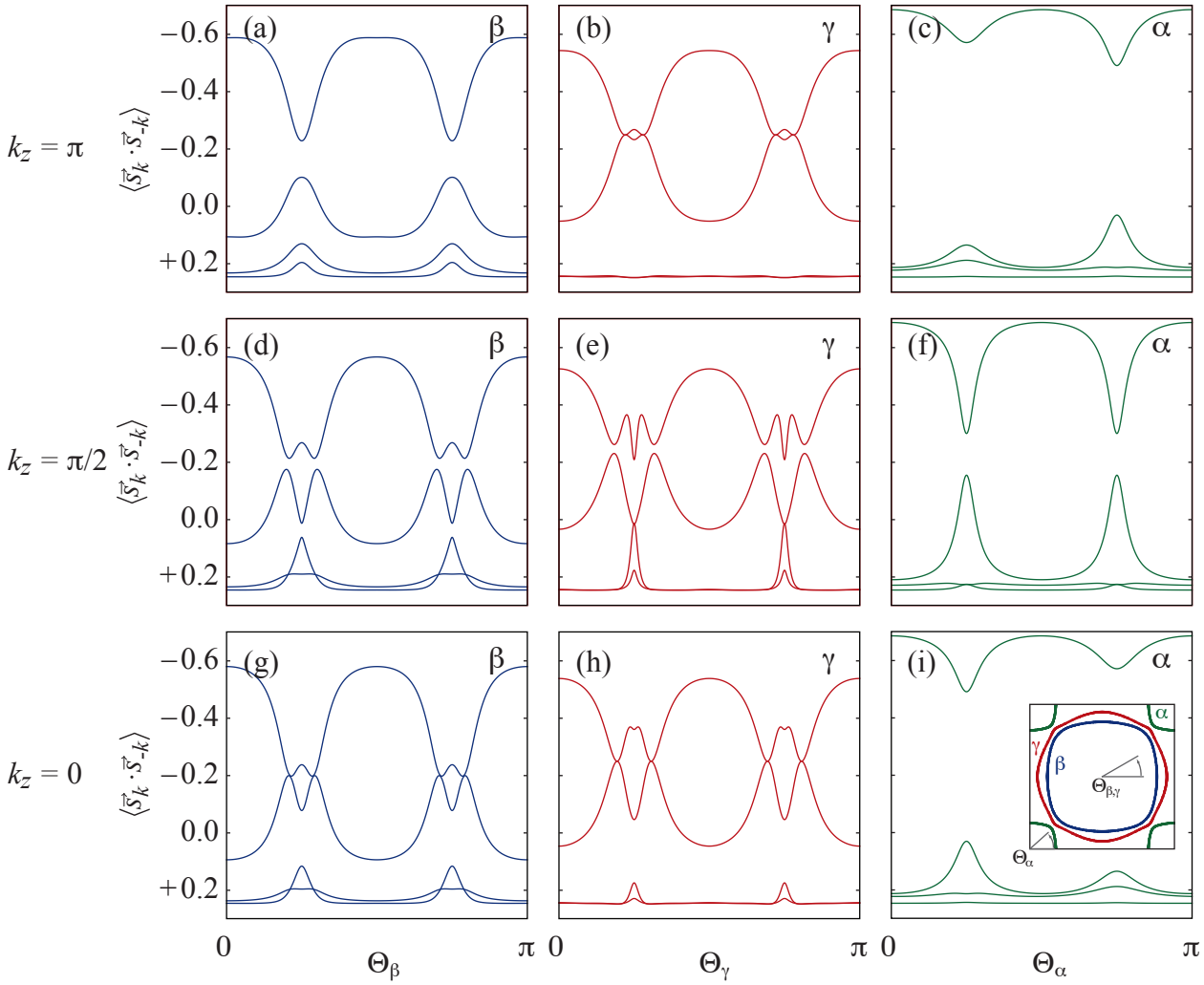

Figure S5: $\langle \vec{s_k} \cdot \vec{s_{-k}} \rangle$ between two states with opposite momentum on the Fermi surface sheets in Sr_2RuO_4 for the β (a,d,g), γ (b,e,h), and α (c,f,i) bands at $k_z = 0$ (g-i), $\frac{\pi}{2}$ (d-f), and π (a-c). The location in the k_x–k_y plane is defined by the angle Θ for each band, as illustrated in the inset at lower right.

References

[1] Veenstra, C. N. *et al.* Determining the Surface-To-Bulk Progression in the Normal-State Electronic Structure of Sr_2RuO_4 by Angle-Resolved Photoemission and Density Functional Theory. *Phys. Rev. Lett.* **110**, 097004 (2013).

[2] Osterwalder, J. Spin-polarized photoemission. *Lect. Notes Phys.* **697**, 95 (2006).

[3] Andersen, O. K. & Saha-Dasgupta, T. Muffin-tin orbitals of arbitrary order. *Phys. Rev. B* **62**, R16219 (2000).

[4] Damascelli, A. *et al.* Fermi surface, surface states, and surface reconstruction in Sr_2RuO_4. *Phys. Rev. Lett.* **85**, 5194–5197 (2000).

[5] Cleveland, W. Robust locally weighted regression and smoothing scatterplots. *Journal of the American Statistical Association* **74**, 829–836 (1979).